Atmos. Meas. Tech., 8, 1183–1195, 2015
www.atmos-meas-tech.net/8/1183/2015/
doi:10.5194/amt-8-1183-2015

Atmospheric Measurement Techniques
Open Access

A new electrodynamic balance (EDB) design for low-temperature studies: application to immersion freezing of pollen extract bioaerosols

H.-J. Tong[1], B. Ouyang[1], N. Nikolovski[2], D. M. Lienhard[1], F. D. Pope[3], and M. Kalberer[1]

[1]Centre for Atmospheric Science, University of Cambridge, Lensfield Road, Cambridge, CB2 1EW, UK
[2]Department of Biochemistry, University of Cambridge, Tennis Court Road, Cambridge, CB2 1QW, UK
[3]School of Geography, Earth and Environmental Sciences, University of Birmingham, Edgbaston, Birmingham, B15 2TT, UK

Correspondence to: F. D. Pope (f.pope@bham.ac.uk)

Received: 17 June 2014 – Published in Atmos. Meas. Tech. Discuss.: 28 July 2014
Revised: 16 December 2014 – Accepted: 1 February 2015 – Published: 10 March 2015

Abstract. In this paper we describe a newly designed cold electrodynamic balance (CEDB) system, built to study the evaporation kinetics and freezing properties of supercooled water droplets. The temperature of the CEDB chamber at the location of the levitated water droplet can be controlled in the range −40 to +40 °C, which is achieved using a combination of liquid nitrogen cooling and heating by positive temperature coefficient heaters. The measurement of liquid droplet radius is obtained by analysing the Mie elastic light scattering from a 532 nm laser. The Mie scattering signal was also used to characterise and distinguish droplet freezing events; liquid droplets produce a regular fringe pattern, whilst the pattern from frozen particles is irregular. The evaporation rate of singly levitated water droplets was calculated from time-resolved measurements of the radii of evaporating droplets and a clear trend of the evaporation rate on temperature was measured. The statistical freezing probabilities of aqueous pollen extracts (pollen washing water) are obtained in the temperature range −4.5 to −40 °C. It was found that that pollen washing water from water birch (*Betula fontinalis occidentalis*) pollen can act as ice nuclei in the immersion freezing mode at temperatures as warm as −22.45 (±0.65) °C. Furthermore it was found that the protein-rich component of the washing water was significantly more ice-active than the non-proteinaceous component.

1 Introduction

At subzero temperatures, water is observed in clouds as both supercooled water droplets (SWDs) and ice particles (Mason, 1975; Cantrell and Heymsfield, 2005). In the absence of ice nuclei (IN), cloud droplets can be supercooled down to temperatures that approach the homogeneous freezing point ∼ −38 °C, which is dependent on droplet size (Sassen, 1985; Rauber and Tokay, 1991; Hogan et al., 2004). The evaporation kinetics, and hence droplet size, of SWDs influences the lifetime and radiative properties of clouds and in particular mixed-phase clouds; it can also affect the likelihood and rate of precipitation (Rosenfeld and Woodley, 2000; Lohmann and Feichter, 2005).

At temperatures above the homogenous freezing point, the heterogeneous freezing of SWDs is caused by interaction of IN-active aerosols with SWDs. Several distinct mechanisms exist, including the deposition, immersion, condensation, and contact modes of freezing (Pruppacher and Klett, 1997). Recently there has been an intense research effort to determine the efficiencies and relevance of the different modes of freezing (e.g. Murray et al., 2010; Knopf et al., 2011; Kanji et al., 2013; Hoffmann et al., 2013a; Atkinson et al., 2013.) Summaries of previous results, obtained by both laboratory work and fieldwork, and the atmospheric implications of these studies are provided by several recent review articles, and no further detail is given here (Laaksonen et al., 1995; Pöschl, 2005; Hoose and Möhler, 2012; Murray et al., 2012; Ladino Moreno et al., 2013). It is noted that several studies suggest that IN processes are still not sufficiently

understood for satisfactory global modelling (e.g. Hoose et al., 2010; DeMott et al., 2010). The most important types of aerosol particles to act as IN are reported to be mineral dust and primary biological aerosols (PBAs), with these two aerosol groups accounting for more than 80 % of ice-crystal residues (Pratt et al., 2009). PBAs are typically large in size (mainly supermicron), and they often dominate the measured mass loading of atmospheric aerosol. However, their number density concentration is small and usually dwarfed by other aerosol types except in the most pristine environments (Griffiths et al., 2012). PBA species include pollen, bacteria, fungal, algae, moss and fern spores, viruses, and fragments of animals and plants (Deguillaume et al., 2008, Moller et al., 2008, Després et al., 2007, Möhler et al., 2007). The atmospheric transport, and hence dispersal, of pollen requires meteorological conditions to produce uplift of pollen-containing air. Atmospheric removal of pollen is determined by the wet and dry deposition rates. The dry deposition is controlled by the settling speed of the pollen grain, which is a function of particle density and size (Aylor, 2002). Both computer modelling and field studies have shown that pollen is capable of travelling large distances and can remain airborne on the order of days (Rousseau et al., 2003; Sofiev et al., 2006; Helbig et al., 2004; Heise and Heise, 1948).

Previous work in our group has used the environmental scanning electron microscope (ESEM) and warm EDB systems to measure the hygroscopicity and hence the warm cloud condensation nuclei (CCN) ability of pollen grains (Pope, 2010; Griffiths et al., 2012). Within liquid water, such as in rain droplets, pollen grains are observed to burst, thereby releasing smaller material – such as sugars, macromolecules, and allergens – into solution (Yttri et al., 2007; Schäppi et al., 1999; Pummer et al., 2012; Augustin et al., 2013).

Pollen grains have been found to be IN-active. Within the condensation freezing mode pollen can initiate freezing events at temperatures up to $-8\,^{\circ}\mathrm{C}$ (Diehl et al., 2001), within the immersion freezing mode at temperatures up to $-9\,^{\circ}\mathrm{C}$ (Diehl et al., 2002), and within the contact freezing mode up to $-5\,^{\circ}\mathrm{C}$ (Diehl et al., 2002). Furthermore, it is found that water that has interacted with pollen grains can also be IN-active in the immersion mode of freezing. This water is referred to as pollen washing water (PWW). In particular, suspended macromolecules within PWW were identified as efficient IN (Pummer et al., 2012; Augustin et al., 2013). Work by the group of Grothe has used two distinct techniques to assess the IN ability of PWW ensembles: firstly freezing events of PWW droplets that are held within emulsions can be observed through use of a microscope fitted with a cryostage (Pummer et al., 2012). Secondly the Leipzig Aerosol Cloud Interaction Simulator (LACIS; Stratman et al., 2004) technique is utilised (Augustin et al., 2013). These results strongly indicate the high IN efficiency of PWW in immersion mode up to $-16\,^{\circ}\mathrm{C}$.

As a robust methodology for the levitation of single particles which carry electric charge, the electrodynamic balance (EDB) technique has been applied in atmosphere science for several decades (see reviews by Davis, 1997; Krieger et al., 2012). On the base of such a strategy, numerous studies have been carried out on aerosol particles and droplets, including but not limited to contact ion pairs formation (e.g. Zhang and Chan, 2000; Lee et al., 2008), hygroscopicity and phase transition (e.g. Tang and Munkelwitz, 1994; Choi and Chan, 2002; Li et al., 2005; Parsons et al., 2006; Pope et al., 2010a; Zobrist et al., 2011), measurement of vapour pressure (e.g. Pope et al., 2010b; Soonsin et al., 2010), oxidation chemistry (e.g. Lee and Chan, 2007; Pope et al., 2010c; Lee et al., 2012), and supercooled droplets and ice nucleation (e.g. Swanson et al., 1999; Krieger et al., 2000; Svensson et al., 2009; Hoffmann et al., 2013a, b; Stöckel et al., 2005). Recently, a new EDB design with concentric cylindrical electrodes was developed to measure the rapid evaporation and condensation process of single droplets (Heinisch et al., 2006, 2009; Davies et al., 2012, 2013).

Using a similar EDB design to Heinisch et al. (2006), we developed and incorporated a new cooling system which is applicable for low-temperature studies. The Heinisch design was chosen because the cylindrical electrodes are mechanically stable and single droplets can be stably confined within a small and well-defined null-point region of the electrodynamic balance whilst gas flows (> 100 sccm) are directed past the droplet (Heinisch et al., 2006; Davies et al., 2012). We describe the new cold electrodynamic balance (CEDB) system, providing particular detail on the cooling strategy. Furthermore, we provide measurement data, from the first applications of this new system: the evaporation rates of supercooled droplets, and the freezing ability of these droplets with and without PWW present. In particular this study provides the first contact-free measurements of ice nucleation of individual PWW droplets.

2 Design and characterisation of new CEDB

The schematic diagram of the new CEDB system is shown in Fig. 1. The system is capable of trapping droplets and following the evolution of the droplet radius under well-defined conditions of temperature and humidity. Evaporation and freezing of droplets are distinguished by following the Mie scattering phase function. The detailed experimental procedure and analysis strategy are detailed.

2.1 Droplet trapping and sizing

The details of the geometrical structure of the EDB chamber, AC and DC electrodes, and the theoretical calculation on the electrodynamic field generated have been reported previously by Heinisch et al. (2009) and Davies et al. (2012) and will be discussed only briefly here. The outer surface

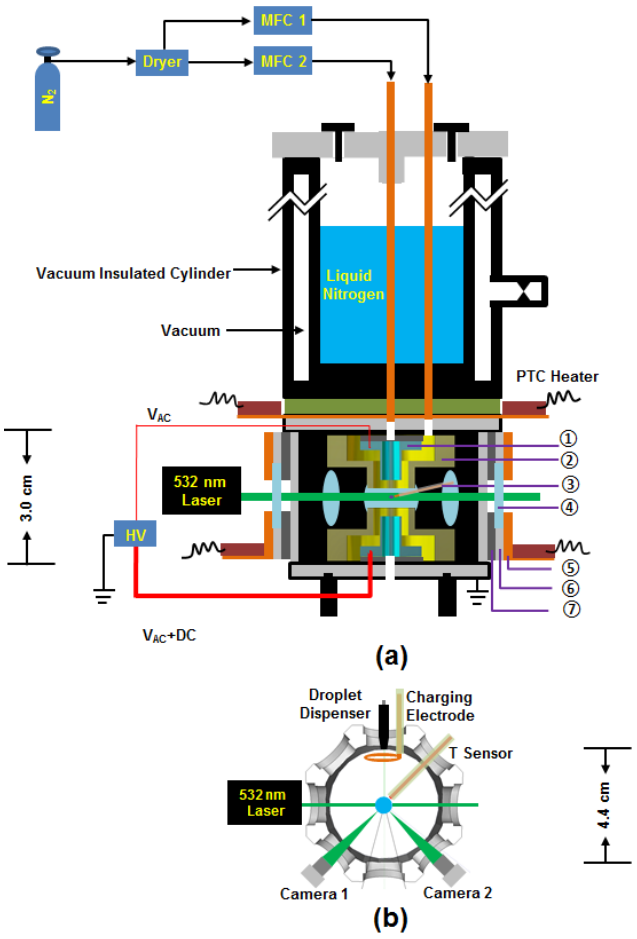

Figure 1. (a) Schematic diagram of the new CEDB system. (1) Inner electrode. (2) Outer electrode. (3) Thermocouple or relative humidity sensor. (4) Glass window. (5) Heating jacket. (6) Holder for glass window. (7) Rubber insulator. **(b)** The top view of the schematic diagram of optical design, dispensing and charging devices, and the thermocouple within the CEDB system. Cameras 1 and 2 are for droplet positioning and Mie scattering observation, respectively.

of the alumina CEDB chamber body has octagonal geometry with an optical port window situated on each flat surface. BK7 glass lenses (Knight Optical, 13 mm in diameter) are mounted in each window to allow passage of light into and out of the chamber. The inner surface of the CEDB chamber has cylindrical geometry with an internal volume of approximately 45.6 cm^3.

As shown in Fig. 1, the cylindrical electrodes are composed of two inner (cyan colour, (1)) and two outer (yellow colour, (2)) copper electrodes. The inner electrodes are 10 mm long have with inner diameter of 2 mm. The inner diameter and length of the outer electrodes are 8 and 13 mm, respectively. The outer electrodes are directly mounted on the stainless-steel base of the CEDB chamber and grounded. The inner electrodes are also mounted on CEDB bases. However, the inner electrodes are electrically insulated from the outer electrodes as well as the metal bases by using a 1 mm thick rubber insulator. After stable mounting of the four electrodes, the distances between the upper and lower electrodes are 8 mm for the inner electrodes and 4 mm for the outer electrodes.

The combined DC and AC electric field ($V_{AC} + V_{DC}$) is generated using Labview software that is transferred through a digital-to-analogue converter and amplified using a high-speed and high-voltage amplifier module (AP-1B3, Matsusada Precision Inc.). The DC voltage applied to upper inner electrode can be varied between −200 and 0 V, the AC voltage between 0 and 1 kV, and the AC frequency between 10 and 300 Hz. The lower-inner electrode has the same AC input applied to it as the upper-inner electrode but without the DC coupling.

Droplets were delivered into the CEDB using a droplet dispenser, which is optimised for low-temperature conditions (MicroFab, 30 (MJ-ABP-01) or 100 (MJ-AB-01) µm orifice diameter). When the same dispenser parameter settings (pulse width, frequency, amplitude etc.) are used, the generated droplets are of high reproducibility with radius fluctuation smaller than 0.5 µm. Within this study the use of different parameter settings led to slight differences in initial SWD size. From the dispenser the droplets follow a trajectory past a charging electrode which is held at 900 V (generated from a Brandenburg 476R high-voltage photomultiplier power supply), thereby allowing the droplet to pick up sufficient charge for trapping. Subsequent to the charging electrode, the droplets pass into the centre of the CEDB chamber, where the droplets are trapped in the null point of the electrodynamic field.

The procedure for the size calibration of the droplet is the same as we previously used (Pope et al., 2010b). A continuous-wave 532 nm wavelength laser (532GLM20, Changchun Dragon Lasers Co., Ltd), with a power of ∼ 20 mW, illuminates the trapped spherical droplet, thus generating Mie scattering resonances. These resonances were recorded over a 21° window, as measured by the angle subtended from the null point to the edges of the window port, using a monochrome complementary metal oxide semiconductor camera (Thorlabs, DCC1545M) centred at ∼ 135° relative to the forward direction of the laser. The particle size obtained by Mie scattering was calibrated using dry soda lime glass sphere standards of the following diameters: 19.3 ± 1.0, 30.1 ± 1.1, and 42.3 ± 1.0 µm (Thermo Scientific Duke Standards, 9020, 9030, 9040). Thousands of soda lime spheres are transformed from stock vial into a syringe needle first. Then the needle containing the spheres is connected with a syringe which is full of air. Continually the spheres are injected into the CEDB chamber by squeezing the air out from the syringe in less than 1 s. Once a particle is trapped, the Mie scattering function is recorded automatically by the camera. Afterwards, the calculated result based on Eq. (1) (Glantschnig and Chen, 1981), which is based on Mie the-

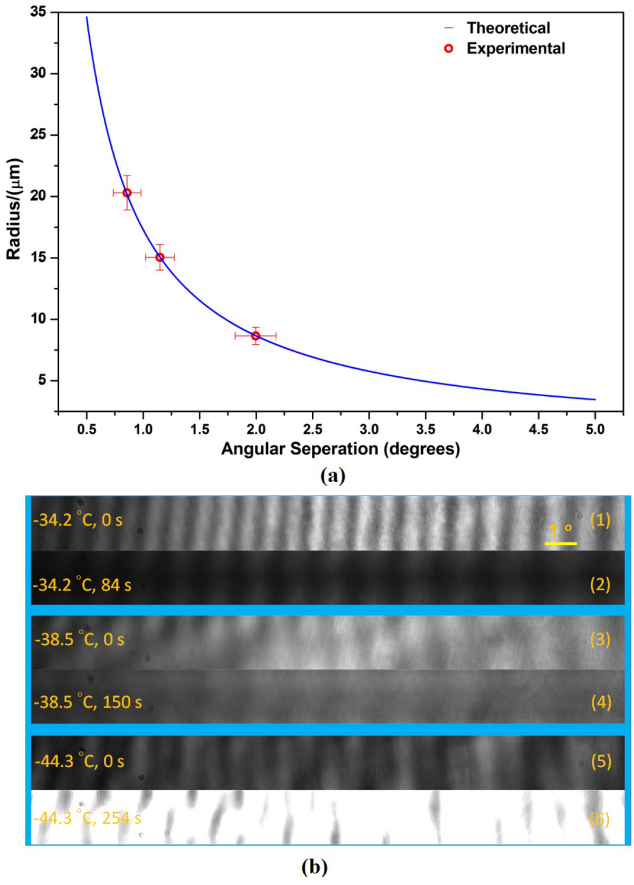

Figure 2. (a) Measurement of particle radius by elastic Mie scattering. The size calibration is achieved using calibrated soda lime spheres. Blue line represents the calculated size based on the peak-to-peak spacing using Eq. (1). The experimental points (red circles) are the measured peak-to-peak separations in the recorded diffraction patterns against the quoted size. The uncertainty in the angular separation is the standard deviation (1σ) in the measurement, and the uncertainty in size is the standard deviation in particle size stated by the manufacturer. **(b)** Mie scattering of pure SWDs at three different temperatures: −34 °C, Eqs. (1) and (2); −38.5 °C, Eqs. (3) and (4); and −44.3 °C, Eqs. (5) and (6). Droplets at −38.5 and −44.3 °C are homogeneously nucleated with irregular scattering patterns. The angular scale bar is the same for all the images.

ory (Mie, 1908), will be compared to the experimentally determined peak-to-peak average of the recorded resonances. The position of the camera for collecting the Mie scattering signal is optimised according to the standard deviation of the theoretical and experimental values. The excellent agreement between the experimental calibration data and the theoretical calculations is shown in Fig. 2. Labview 11 software was used for experimental control and data acquisition.

$$\Delta\theta \cong \frac{\lambda}{r}\left(\cos\frac{\theta}{2} + \frac{n\sin\frac{\theta}{2}}{\sqrt{1+n^2-2n\cos\frac{\theta}{2}}}\right)^{-1} \quad (1)$$

In Eq. (1), λ is the illuminating laser wavelength (532 nm). n is the refractive index of trapped droplet (the value of 1.33 will be used in this study for pure water), θ is the median angle of observed phase functions, and $\Delta\theta$ is the angular separation.

We have characterised the trapping ability of CEDB under three different flow regimes:

i. Stagnant conditions with no gas flow through the electrodes provide the most stable trapping. As no downward force from the gas flow though the CEDB is present, a particle can be trapped (by a symmetric electrical field) in a short time with a high trapping success rate. In addition it is observed that the particle can be moved up and down by the DC voltage freely under stagnant conditions. Whilst stagnant conditions produced conditions beneficial to stable trapping, trapping temperatures < -30 °C could not be achieved. Hence further experiments were not performed under stagnant conditions because temperatures as low as the homogenous freezing temperature were required for the experiments described below.

ii. When gas is flowing through both cooling lines (controlled by mass flow controller (MFC) 1 and 2 in Fig. 1a), a relatively large cross-sectional area of ca. 50 mm^2 of near-constant gas flow velocity is generated within the CEDB. This uniform flow facilitates the stable trapping of particles over long timescales as they experience the same flow forces regardless of small radial oscillations which can occur within the CEDB due to the changing size of the particle during an experiment. Flow rates of 50 and 200 sccm for the inner flow and outer flow, respectively, provide such stable conditions.

iii. The least stable trapping conditions were found when gas was only passed through the inner electrode as this resulted in a much smaller cross-sectional area (ca. 3 mm^2) with uniform flow conditions. Consequently only flow rates up to 10 sccm could be used in this configuration.

2.2 Cooling strategy of CEDB

To cool the CEDB system, a 300 mm long and 50 mm inner diameter vacuum-insulated liquid nitrogen Dewar was attached to the top of the CEDB. This Dewar consists of double-walled liquid nitrogen steel reservoir with a vacuum held between the two walls. The thickness of the Dewar wall and vacuum layer are larger than 1 and 5 mm, respectively. To further reduce heat exchange between the liquid nitrogen Dewar and the ambient atmosphere, the outer surface of the liquid nitrogen cylinder is covered with flexible synthetic rubber insulation (Insul-Tube and Insul-Sheet, NMC (UK) Ltd) with a thickness of ∼9 mm. The top of the Dewar is sealed with a polytetrafluoroethene (PTFE) cap which is also

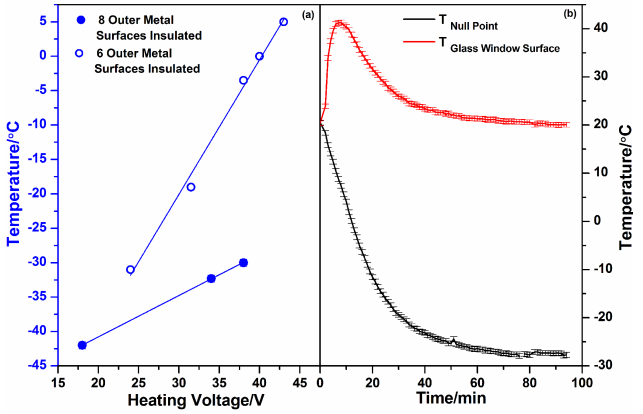

Figure 3. Temperature characterisation curves for the null-point region of the CEDB. Two different insulation schemes allow access to different temperature ranges in the EDB. **(a)** Final temperature reached when eight outer metal surfaces (blue solid circles) or six outer metal surfaces are insulated (blue circles) CEDB chamber versus heating voltage. **(b)** An example of glass window surface (red line) and null-point (black line) temperature reaching −28 °C with 24 V heating voltage.

insulated with synthetic rubber. The vacuum and insulation material significantly reduce the evaporation of liquid nitrogen. Additionally, the liquid nitrogen is refilled periodically, thereby increasing the temperature stability within the CEDB chamber (fluctuation is < 0.2 °C after equilibrium).

The CEDB chamber is cooled by flowing N_2 gas through two copper heat exchange tubes (3 mm outside diameter). The pipes pass through the liquid nitrogen Dewar and direct the gas flows through the upper electrodes (see Fig. 1). The gas flow from the central pipe passes through the upper-inner electrode and directly passes through the null-point region of the CEDB. The gas flow from the outer pipe is directed through the gap formed between the inner and outer-upper electrodes and acts as an additional cooling sheath gas as described above. The gas flows are controlled using mass flow controllers (Brooks Smart MFC, Brooks Instruments) and are normally set to ∼ 80 sccm for the outer pipe (MFC 1 in Fig. 1) and 20 sccm for the central pipe (MFC 2 in Fig. 1). These flow rates are both laminar and matched in downward velocity. The Reynolds number of the two gas flows can be calculated with Eq. (2), where d is diameter of inner (0.002 m) or outer electrode (0.004 m). u is the mass flow velocity (m s^{-1}). ρ is the density (1.13 kg m^3 for nitrogen gas). η is the dynamic viscosity (1.75×10^{-5} pa s for nitrogen gas at 20 °C). The calculated Reynolds numbers at 20 °C are 27.4 and 13.7 for the 80 and 20 sccm flow rates, respectively. These low Reynolds numbers comfortably ensure laminar flow at all temperatures investigated in this study.

$$Re = \frac{du\rho}{\eta} \quad (2)$$

The temperature at the null point of the CEDB is controlled by varying the temperature of the CEDB chamber wall using variable heaters (HP05-1/10-24, Onecall). The null-point temperature and radial temperature gradient are measured using a 0.1 °C resolution thermometer (HH 308, Omega) with type K thermocouples. A temperature calibration curve for the null-point position is shown in Fig. 3a. It can be seen that the null-point temperature varies linearly with the DC voltage that is supplied to the heater. This configuration allows for easy control of the null-point temperature between −40 and 0 °C. When insulating all eight outer metal surfaces of the CEDB chamber with a 4 mm depth rubber insulator, the null-point temperature can be controlled from −30 to −42 °C with a heating range from 17 to 38 V. If only six outer metal surfaces are insulated, the null-point temperature can be regulated from 40 to −31 °C with a heating range from 24 to 43 V. Only the calibration curve ranges from 5 to −42 °C are shown in Fig. 3. This configuration sets up a radial temperature gradient within the cell at the height of the null point. As a result of the diffusional mixing of the cold and warm gases, it will colder upstream of the null point than downstream; the null-point temperature will be at an intermediate temperature. The temperature gradients were measured by accurately positioning a thermocouple (5SC-GG-(K)-30-(36), max ±2.2 °C) in the cell, as shown in Table 1 for five temperatures at the null point from −5 to −42 °C. Although the maximal accuracy of the thermocouple is ±2.2 °C, we also calibrated with a TSP01-USB temperature and humidity sensor (±0.5 °C Thorlabs) in the temperature range −15 to 25 °C. The difference of the two kinds of sensors is smaller than 0.1 °C in the whole range. Additionally, temperature of the liquid nitrogen is observed to be −194 °C with the K type thermocouple, which is quite close to the boiling point of liquid nitrogen (Haynes, 2013). Hence we suggest the thermocouple we used is reliable. Temperature gradients in the axial directions (above and below the null point) were < 3 °C mm^{-1}, and radial gradients of < 1 °C were measured throughout the temperature range. During the experiment, the trapped particles are always confined at the null point (±1 mm) by adjusting controlling AC or DC parameters with the feedback program within the Labview (as discussed in Sect. 2.1). Thus, we are confident that the trapped particle will not deviate significantly in any direction from the null point.

The relative humidity (RH) at the null point can get < 0.2 % (EK-H5 kit with SHT75 humidity sensor, Sensirion) when the temperature is higher than −20 °C, and < 0.7 % when the temperature reaches ∼ −40 °C. The standard RH deviation of the SHT75 probe is ∼ ±4% at 0 % RH. Figure 3b provides an example of the time required for the temperature of both the CEDB null point and the outer glass window surface to reach steady state.

The current instrument design only allows performing experiments at low RH due to the gas flow passing through the liquid nitrogen reservoir. Higher RH conditions in the CEDB

Table 1. Temperature gradients around the null point of the CEDB

$T_{\text{null point}}$/°C	$T1$/°C	$T2$/°C	$T3$/°C
−41.9	−46.2	−36.2	−39.8
−36.5	−39	−1.8	−4.2
−25.7	−28.7	−22.2	−23.9
−13.1	−15	−7.2	−11.4
−5.2	−8.2	−0.55	−4

$T1$: Temperature 2 mm above the centre,
$T2$: Temperature 2 mm below the centre,
$T3$: Temperature 2 mm radially away from the centre.

could be reached by cooling the copper tubes less by insulating the copper tubes in the liquid nitrogen reservoir, by using higher-temperature coolants, or by introducing a separate humidified gas flow. The capability to adjust the RH will be integrated in the next version of our CEDB.

In order to stop the formation of condensation and/or freezing on the outer surface of the glass windows, a rubber insulator ((6) in Fig. 1) was used between the window and metal body of the chamber. Furthermore, the outer surface of the glass window was warmed by a heating jacket ((4) in Fig. 1). The jacket was designed so the outside face of the window could be exposed to the laboratory air. Such a design allows for the easy alignment of the laser into the chamber and through the CEDB null point. When the outside surface temperature of the glass windows was lower than 15 °C, a dry laminar air flow is also directed onto the surface to avoid water condensation and to maintain the transparency of the window.

In order to quantify the CEDB temperature for low-temperature application, we observed the homogeneous ice nucleation of pure supercooled water droplets. We found the Mie scattering pattern of SWDs becomes highly irregular at -38 ± 1 °C (see example data in Fig. 2b), which corresponds to the homogeneous ice nucleation of SWDs. This is in good agreement with established literature values (Koop et al., 2000).

3 Results and discussion

The first applications of the new CEDB system, detailed in this paper, are in the study of the evaporation kinetics of SWDs and the immersion freezing ability of PWW droplets.

3.1 Evaporation kinetics of supercooled water droplets

As the main application of the CEDB, in this paper, will be the investigation of freezing events of aqueous droplets, it is necessary to characterise the evaporation rate of SWDs, which defines the time window accessible for the freezing studies.

The mean free path of N_2 gas (λ_{N_2}) at subzero temperatures and atmospheric pressure is less than 58.8 nm (Hirschfelder et al., 1954). Considering that the measured droplet radius (r) is always greater than 2.5 µm, the Knudsen number, $Kn = \lambda_{N_2}/r$, is always much smaller than 1; therefore the N_2 gas flow is always in the continuum regime (Seinfeld and Pandis, 1998). Hence both the mass transfer of water molecules from the SWD surface to the surrounding N_2 atmosphere and the heat transfer is significant in influencing the kinetic evaporation rate of the trapped SWDs (Miles et al., 2012; Holyst et al., 2013). Due to the influence of heat transfer, the surface temperature of SWDs will be lower than the surrounding gas flow, and this reduces the observed evaporation rate. It is noted that, under dry conditions such as in our setup, the colder the surrounding gas flow, the smaller the temperature difference between the droplet surface and the gas phase (Kulmala et al., 1993; Miles et al., 2012). The gas flow rate through the CEDB chamber can influence the evaporation rate due to the effects of Stefan flow (Davies et al., 2014); however this effect is calculated to be negligible in the CEDB system and will not be discussed further here.

To ensure that the nitrogen gas was as dry as possible, the flow from the cylinder was passed through a 300 mm long, and 50 mm in diameter, drying tube containing silica gel particles (Breckland Scientific Supplies Ltd). Any remaining water vapour in the gas flow is caught in the cold trap formed by copper tubing heat exchangers which are held at nearly liquid nitrogen temperature (−196 °C). Considering the saturation vapour pressures of liquid water and ice at ∼ −150 °C (123 K) are 3.02×10^{-9} and 8.50×10^{-10} Pa, and the vapour pressure decreases as the temperature lowers (Murphy and Koop, 2005), we assume that the evaporation of SWDs in the present study occurs under a dry environment. High-pressure liquid chromatography (HPLC) grade water (RH1020, Rathburn Chemicals Ltd) was used to generate the water droplets. Pure water droplets were only injected into the CEDB chamber once the null-point temperature had stabilised to the desired temperature.

The evaporation rates of SWDs recorded at −18.8 (±0.6), −22.7 (±0.6), −28.0 (±0.6), −32.1 (±0.6), and −34.2 (±0.6) °C, as measured by the change in radius, are shown in Fig. 4a. This figure indicates that under dry nitrogen gas flow the evaporation rate of SWDs decreases as temperature of the null point decreases, as expected, because of the decreasing water vapour pressure. The evaporation rate of SWDs can be parameterised by determining the time taken for the droplet to evaporate to half of its initial radius ($t_{r1/2}$). As expected it is observed that the evaporation rates of SWDs increase with the initial size of the SWDs because of the greater number of water molecules transferred from liquid to gas phase. An alternative parameterisation is the ratio of $t_{r1/2}$ to the initial radius of the droplet ($t_{r1/2}/R$), which is used to minimise the influence of initial SWD size as shown in Fig. 4b. This parameterisation strategy has been previously used as an empirical tool to estimate the mass transfer of water molecules in glassy aerosol droplets (Tong et al., 2011).

Although in this study we do not quantify the influence of mass and heat transfer on the evaporating rate of SWDs,

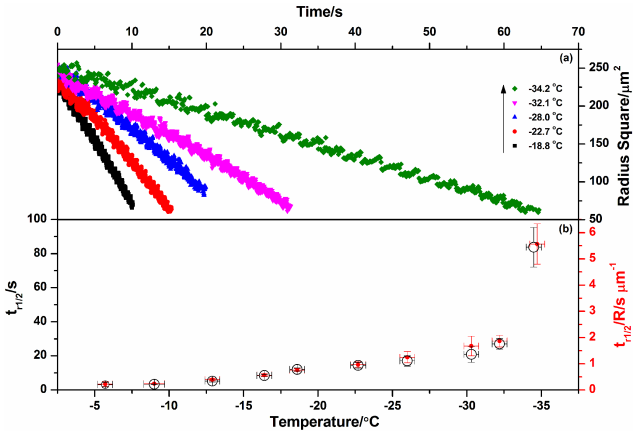

Figure 4. (a) Example evaporation decay traces of SWDs at five different subzero temperatures. **(b)** $t_{r1/2}$ of SWDs at 10 different temperatures (black circles), and the ratio of $t_{r1/2}$ to radius ($t_{r1/2}/R$) estimated for the change of SWDs for a series of temperature measurements (red dots). The temperature error is the value stated by the manufacturer. The y error for the $t_{r1/2}$ and $t_{r1/2}/R$ is the standard deviation of the measurement. At least three individual experiments at each temperature were conducted.

these results show that SWD evaporation kinetics can be measured using the new CEDB design described in this paper, at temperatures as low as the homogenous freezing temperature. This study will form the basis of a forthcoming paper.

Importantly for the upcoming discussion on heterogeneous freezing, we conclusively demonstrate that water droplets with an initial radius of $\sim 15\,\mu m$ can be trapped for ca. 10–60 s within a ~ 100 sccm pure nitrogen gas in the temperature range from -5.7 to $-34.5\,^{\circ}C$, thus defining the timescale available for freezing experiments in the current CEDB setup.

3.2 Immersion freezing of PWW solution

The extraction procedure for the PWW solutions, which is illustrated in Fig. 5a, is similar to the procedure used by Augustin et al. (2013). Briefly, water birch pollen (*Betula fontinalis occidentalis*), which was obtained as a dried sample from Sigma-Aldrich (P6895-1G), was suspended in water at a mass concentration of $5\,g\,mL^{-1}$ and stirred for ~ 1 min using a mixer (Fisher Scientific Top Mix FB 15024). After stirring, the suspension was then stored in a refrigerator for 24 h. The solution was then stirred again and filtered through sequential use of 0.45 and 0.2 μm pore filters (Supelco, 4 mm, PTFE membrane). In this aspect the procedure differed from that of Augustin et al., which used filters of size 4–7 μm. After the filtration, the PWW solution is observed to be transparent but with a bright yellow hue. Each filtered PWW solution was used within 4 days of preparation to minimise the risk of contamination. The mass fraction (f_{PWW}) of biological material within the PWW solution is obtained by measuring the mass of the extracted PWW solution and mass of the dried residue with a 0.1 mg accuracy balance (Fisherbrand PS-60). Dry PWW residues were obtained by evaporating the PWW solutions under nitrogen gas (Air Liquide UK Limited, > 99.999 %) and subsequent heating within an oven (Memmert, ULM 400) at a temperature < 95 °C for more than 4 h.

Figure 6 provides the calibration curve for the mass fraction of biological material in solution versus initial concentration of pollen mass in the extraction solution. Furthermore, the refractive index of the PWW solution is measured using a refractometer (RFM340, Bellingham + Stanley Ltd), also shown in Fig. 6. Figure 6 clearly indicates that the mass fraction of PWW solutions (f_{PWW}) increases from 0.000135 to 0.0129 as the pollen suspension concentration (W_{pollen}) increases from 1 to $50\,mg\,mL^{-1}$ (pollen mass per water volume). The upper threshold, $f_{PWW} = 0.0129$, in this study is similar to mass fractions used in the study of Pummer et al. (2012). However, within the experiments described in this study, the values of f_{PWW} will increase as the water content of the PWW droplets evaporate. The refractive index of PWW solutions (RI_{PWW}) increases from 1.332905 (pure water) to 1.33543 as the pollen suspension concentration increase from 0 to $50\,mg\,mL^{-1}$. To calculate the particle size, via Eq. (2), we used the refractive index value of pure water ($n = 1.33$) in all cases. For a 15 μm (in radius) PWW droplet, without considering the density evolution of it during the evaporation process, at most this simplification led to an overestimation of the initial droplet size by ~ 0.28 %, and 0.54 % for the same droplet at time $t_{r1/2}$.

Freezing events of the PWW droplets are identified by the change in the elastic Mie scattering signal. Liquid droplets are spherical and produce regular fringe patterns, whilst frozen solid particles are non-spherical and produce irregular patters. Such a strategy for distinguishing liquid and frozen droplets has been successfully demonstrated previously (e.g. Krämer et al., 1999; Shaw et al., 2000; Vortisch et al., 2000). Examples of different phase functions are shown in Fig. 5 panels b, c, d, and e. In particular, Fig. 5b provides images of scattered light recorded at 1.3 and 10 s after capture in the EDB trap from a PWW droplet at $-21.8\,^{\circ}C$; the reduction in fringe spacing clearly indicates that the droplet has lost some of its water content through evaporation but has not frozen. Figure 5c provides images of the scattered light recorded immediately after trapping (0.0 s) and 5.0 s after injection for a frozen PWW droplet at $-24.2\,^{\circ}C$; both phase functions are irregular, indicating that this droplet was frozen almost instantaneously within the trap. Figure 5d shows the phase functions of a trapped PWW 0.4 and 2.6 s after injection; the first phase function is regular and the second is irregular, indicating that a freezing event happened after a short period of evaporation. Figure 5e provides the phase functions, at 0 and 60 s after injection, for a PWW which freezes instantaneously at $-32.2\,^{\circ}C$.

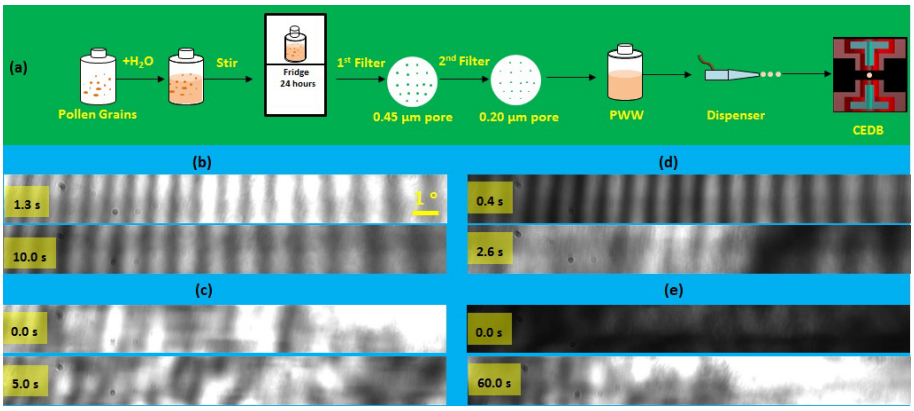

Figure 5. Extraction procedure and example phase-dependent elastic Mie scattering images. **(a)** Drawings of the extraction procedure of PWW solutions. **(b)** The phase function of an evaporating PWW particle at −21.8 °C and recorded at 1.3 (top) and 10.0 s (bottom). **(c)** The irregular phase functions of a PWW particle that froze immediately after injection at −24.2 °C. **(d)** The recorded phase functions of a PWW particle that froze after a very short delay at −24.2 °C. **(e)** The irregular phase functions of a PWW particle that froze immediately after injection at −32.2 °C. The angular scale bar (shown in **b**) is the same for all the images.

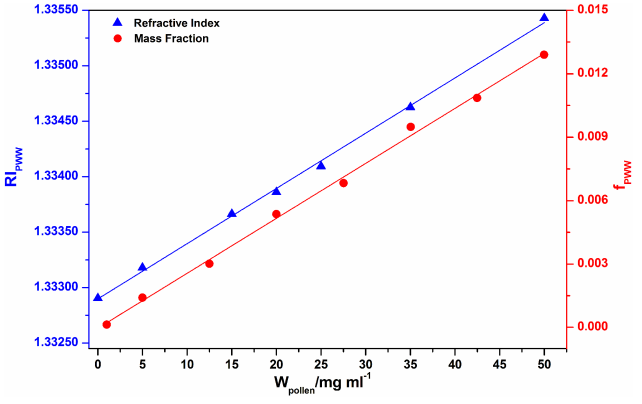

Figure 6. The mass fraction (f_{PWW}, red circles) and refractive index (RI_{PWW}, blue triangles) of PWW solutions versus the pollen suspension concentration (W_{pollen}). The red and blue lines are linear fits to the data with adjusted-R^2 values of 0.9969 and 0.9981, respectively.

To test the freezing efficiency of PWW solution droplets, experiments were performed at 10 different temperatures. The temperature-dependent freezing fractions (f_{ice}) of the PWW droplets were calculated using Eq. (3):

$$f_{ice} = \frac{N_f}{N_0}, \quad (3)$$

where N_f is the number of PWW droplets that freeze, and N_0 is the total number of PWW droplets. The coldest temperature the droplet encounters, as it travels radially from the dispenser to the null point, is found at the null point (see Table 1). It is noted that the particle could have frozen at a warmer temperature encountered earlier in its trajectory from dispenser to null point. However, this does not affect the measurement of ice fraction (f_{ice}) for a given temperature since the probability of freezing always increases with decreasing temperature. A total of 30–158 droplets were analysed at each temperature (as shown in Fig. 7). At the highest and lowest temperatures fewer droplets were required for good statistics. A greater number of droplets were measured in the temperature region where the value of f_{ice} is evolving rapidly. The numbers of PWW droplets used were 158 for −15.2 (±0.7) °C, 82 for −18.8 (±0.85) °C, 151 for −20.5 (±0.65) °C, 104 for −22.5 (±0.65) °C, 125 for −24.2 (±0.65) °C, 100 for −27.5 (±0.5) °C, 50 for −30.5 (±0.5) °C, and 60 for −32.2 (±0.5) °C.

The ice freezing fraction of droplets initially generated from 5 and 47 mg mL^{-1} PWW solution is shown in Fig. 7. It is noted that the PWW droplet surface temperature will be lowered with the heat transfer effect. As the droplet water evaporates, the concentration of the non-volatile biomaterial within the droplet will become more concentrated. However, in droplets where freezing was observed, the freezing occurred within 0.3 s after injection of the PWW droplets into the trap. In this short time window the droplets do not evaporate significantly; see Fig. 4a. In a very small number of PWW droplets (< 5 %) freezing occurred after 0.3 s, but these droplets were not considered in the data analysis shown in Figs. 7 and 8. We conclude that within the time resolution of the experiment any time dependence associated with Eq. (3) can be ignored.

A clear increasing trend for f_{ice} was observed with decreasing temperature for both the 5 and 47 mg mL^{-1} PWW solution droplets, see Fig. 7. For the 5 mg mL^{-1} PWW, the f_{ice} increases rapidly from 0 to 0.85 as the temperature is lowered from −20.50 (±0.65) to −22.45 (±0.65) °C, and the frozen fraction reaches unity at temperatures ≤ −27.5 (±0.5) °C. The f_{ice} of 47 mg mL^{-1} PWW droplets increase from 0 to 0.06 as the temperature is lowered from −4.50

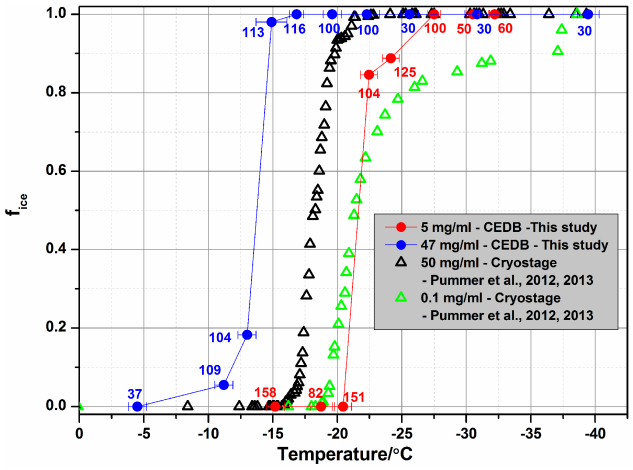

Figure 7. The temperature-dependent freezing fraction (f_{ice},) of 5 (red point and line) and 47 mg mL^{-1} (blue point and line) birch PWW droplets. Data from this study (*Betula fontinalis occidentalis*, CEDB) is compared to the data reported in Augustin et al. (2013) for *Betula pendula* obtained using a cryostage microscope. The temperature error bar is calculated using both the stated probe accuracy from the manufacturer and the fluctuation of experimental temperature for each data point. The number in the figure is the droplet number for each data point.

(±0.65) to −11.20 (±0.65) °C; it then reaches unity at temperatures ≤ −16.85 (±0.55) °C. The results of Pummer et al. (2012) and Pummer et al. (2013), which are presented in Augustin et al. (2013), are also shown in Fig. 7. These studies used a microscope equipped with a cryostage to investigate PWW emulsions of silver birch (*Betula pendula*) (Pummer et al., 2012; Pummer, 2013; Augustin et al., 2013). The CEDB data using 5 mg mL^{-1} water birch (*Betula fontinalis occidentalis*) pollen PWW samples show a similar temperature-dependent trend in f_{ice} to the 50 mg mL^{-1} *Betula pendula* PWW droplets. Both the f_{ice} values for these two different species increase rapidly, from an initial value of ∼0 to 1, in the relatively small temperature range of ∼5 °C. The 0.1 mg mL^{-1} *Betula pendula* PWW droplets also have a similarly shaped f_{ice} curve to the CEDB results but show subtle differences in freezing ability, compared to both the 5 mg mL^{-1} *Betula fontinalis occidentalis* sample and 50 mg mL^{-1} *Betula pendula* sample, with f_{ice} only reaching a value of ∼0.9 before the onset of homogenous nucleation at ∼37.5 °C.

The similarity between the freezing curves of the two different pollen species from the same genus is intriguing; it suggests that the component(s) of PWW responsible for IN activity is common to the *Betula* genus. It should be noted that the pollen grains of both silver birch and water birch have very similar shapes with the characteristic raised pore structure of the *Betula* genus, but it seems unlikely that these macro-features of the pollen structure will have significant influence on the freezing ability on the filtered birch PWW. It has been shown that saccharides, lipids, and proteins are easily removed from pollen particles via aqueous extraction (Pummer et al., 2013). It has been suggested that the IN ability of birch pollen PWW is not due to proteinaceous compounds but rather sugar-like macromolecules with masses between 100 and 300 kDa (Pummer et al., 2012).

The differences between the f_{ice} values of different species are likely due to the different concentrations of the extractable compounds. These differences can even occur across samples from the same genus and species but from different geographical regions (Augustin et al., 2013). We speculate that the yellow colour of the water birch PWW solution might indicates that it contains a high concentration of carotenoids, which may be one of the compounds that could influence the immersion freezing of PWW. It is possible that differences between the CEDB and cryostage measurement techniques may also influence the observed differences: the CEDB measurement used monodisperse (∼ 30 µm diameter) sized PWW droplets, as opposed to the polydisperse PWW droplet size distribution (10–200 µm diameter) of the cryostage experiments by Pummer et al. (2012, 2013). It is noted that for a fixed concentration of PWW the sample volume is important for the freezing of PWW droplets and consequently the reported freezing fraction. In other words, the absolute number of IN-active compounds in larger-volume samples will be higher under the same concentration. Secondly the PWW droplets in the CEDB are charged and cooled over a different timescale compared to the cryostage experiments. Finally the contact-free nature of the CEDB may influence the outcome.

In the real atmosphere bioaerosols will encounter a range of different RHs, within and out of clouds, and PWW will likely go through hydration and dehydration events. In order to investigate the effect of dehydration on the IN ability of PWW, the 5 mg mL^{-1} birch PWW was dehydrated within an oven set at a temperature of 80 °C. Subsequent to this drying step, it was re-dissolved using HPLC grade deionised water. The mass fraction of the PWW before and after dehydration and subsequent rehydration was kept the same at 0.14 %. The freezing fraction of re-dissolved 5 mg mL^{-1} birch PWW is shown in Fig. 8 (blue triangles) and compared to the original 5 mg mL^{-1} PWW that was not subjected to the dehydration step (red circles). The two f_{ice} curves are found to be similar: firstly, the boundary temperature between observed ice nucleation and no ice nucleation PWW not subject to the dehydration step is at −20.5 (±0.7) °C, and for the re-dissolved PWW it is at −16.7 (±0.5) °C. Secondly, the f_{ice} of both the original and re-dissolved 5 mg mL^{-1} birch PWW exceeds 0.8 while lowering the temperature by another 7 °C relative to the boundary temperature. The similarity in observations strongly indicates that dehydration of the sample does not significantly weaken the IN activity of PWW. Such a finding is in agreement with the conclusion by Pummer et al. (2012, 2013) and indicates that under various RH environments the PWW residues will be efficient IN. Hence PWW

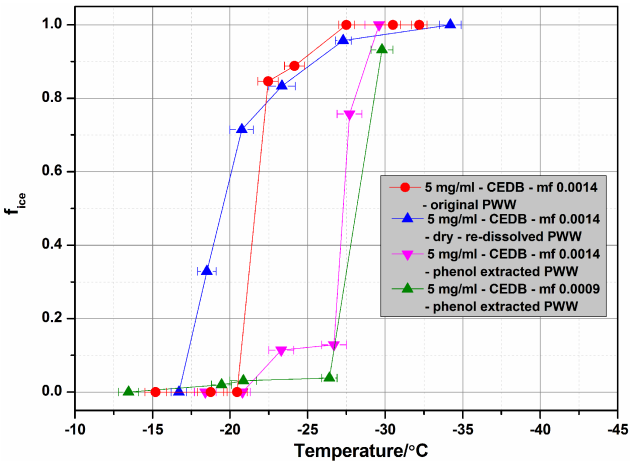

Figure 8. Freezing fraction of 5 mg mL^{-1} birch PWW with and without phenol extraction. Blue triangles: re-dissolved PWW after initial dehydration (mf = 0.0014). Pink triangles: PWW extracted with phenol (mf = 0.0014). Green triangles: PWW extracted with phenol (mf = 0.0009). Red circles are the same data as shown in Fig. 7 (mf = 0.0014).

residue will still be able to influence local precipitation by acting as highly active IN regardless of the RH history they encountered prior to the freezing event.

Pummer et al. (2012, 2013) analysed the IN activity of PWW after protein decomposition and suggested that the polysaccharide content of the PWW might be responsible for controlling the IN activity of PWW. For the purpose of analysing the IN activity of polysaccharides in a more direct way, we used a method similar to Galanos et al. (1969). Water-saturated phenol (Tris-HCl saturated, pH 6.6/7.9, Amresco-Interchim, Biotechnology Grade) was used to remove proteins from PWW (Galanos et al., 1969). Briefly the protocol is as follows: initially 5 mg mL^{-1} birch PWW was generated using the procedure as described above. It was then mixed with water-saturated phenol (1:1 v/v) and stirred by a mixer (Fisher Scientific Top Mix FB 15024) for 5 min. The mixture is then kept in the refrigerator overnight to allow the phenol phase to separate from the aqueous phase. The aqueous phase will now be deficient of the protein fraction which preferentially partitions to the less polar phenol phase. We henceforth refer to this aqueous phase as the "phenol extracted PWW". The mass fraction of the phenol extracted PWW is obtained by performing a dehydration and rehydration once the mass of the residue is known.

The freezing fraction of phenol extracted PWW is shown in Fig. 8 (pink triangle) and compared to the non-extracted PWW. It can be seen that the removal of the proteinaceous component leads to a less effective IN. Interestingly the f_{ice} curve of the phenol extracted PWW can be separated into two distinct stages according to the slope. In the first stage, the value of f_{ice} increases from 0 to 0.11 as null-point temperature lowers from −20.8 (±0.5) °C to −23.3 (±0.8) °C; afterwards a plateau appears as the temperature continually goes down to −26.7 (±0.8) °C with f_{ice} =0.13. In the second stage, the freezing fraction jumps steeply to 0.76 at −27.7 (±0.8) °C and finally up to 1 at −27.7 (±0.8) °C when the temperature arrives at −29.6 (±0.9) °C. Such distinct stages within the f_{ice} curve are indicative of differnet IN species within the PWW. Hence we infer that at least two kinds of IN-active compounds have been left in the water phase after dealing with phenol. These were not observed in the PWW samples because of the greater IN ability of the proteinaceous fraction.

Additionally, we also observed the IN behaviour of lower concentration (mf = 0.09 %) phenol extracted PWW and shown it in Fig. 8 (olive triangle). The signifcant increasing of f_{ice} started from −26.4 °C with a value of 0.13 and increased to 0.76 at −29.8 °C. As expected, this curve indicates that lower concentrations of the polysaccharide-rich material result in a lower IN activity of PWW droplet.

The experimental results presented in this study, in combination with other studies (Pummer et al., 2012; Augustin et al., 2013), indicate that birch PWW droplets are active in the immersion mode of freezing at relatively warm temperatures. Extraction of the proteinaceous component of the PWW indicates that the proteins are likely the most IN-active component of PWW. However the non-proteinaceous component (likely polysaccharides) is still IN-active albeit at a lower temperature. However the freezing temperatures are lower than that observed for birch (*Betula alba*) pollen grains in the contact, immersion, and condensation modes of freezing (Diehl et al., 2001, 2002). The IN activity behaviour shown by the birch PWW suggests significant potential for cloud formation and precipitation especially due to the wide geographical extent of birch.

4 Conclusions

This paper introduces a new design of CEDB. Furthermore it reports the initial applications of this CEDB to measure the evaporation kinetics and freezing properties of SWDs. Accurate size and phase determination of the single levitated SWDs was characterised via measurement of the Mie scattering signal. The rate of evaporation of SWDs in a dry gaseous environment was determined, in the temperature range from −5 to −34.5 °C, and the current setup allows the freezing experiments to be performed within a time window of up to 1 min dependent on temperature. The phase transition of the PWW particle from liquid to frozen solid, and hence the freezing efficiency of PWW, was characterised through the loss of the regular Mie scattering signal from the levitated droplet. From this data, the statistical freezing fractions of PWW droplets were obtained in the temperature range −4.5 to −40 °C. It was found that that PWW from water birch (*Betula fontinalis occidentalis*) pollen, in common with other *Betula* species (Pummer et al., 2012; Augustin et al., 2013), is IN-active in the immersion freezing mode at relatively

warm temperatures: −22 °C and below. The evaporation and freezing results from this study illustrate the versatility of the new CEDB system for studying subzero phenomena in a contact-free technique. The CEDB instrument will be used in future experiments to study a range of freezing phenomena and their implications for atmospheric ice nucleation.

Acknowledgements. This study was supported by NERC via the ACID-PRUF consortium grant (NE/I020105/1). We thank Jonathan Reid and James Davis for providing detailed information about their EDB design. We thank Thomas Leisner for good advice and providing the opportunity to visit his EDB laboratory. We thank Hinrich Grothe and Bernhard Pummer for provision of their PWW data sets.

Edited by: P. Herckes

References

Atkinson, J. D., Murray, B. J., Woodhouse, M. T., Whale, T. F., Baustian, K. J., Carslaw, K. S., Dobbie, S., O'Sullivan, D., and Malkin, T. L.: The importance of feldspar for ice nucleation by mineral dust in mixed-phase clouds, Nature, 498, 355–358, 2013.

Augustin, S., Wex, H., Niedermeier, D., Pummer, B., Grothe, H., Hartmann, S., Tomsche, L., Clauss, T., Voigtländer, J., Ignatius, K., and Stratmann, F.: Immersion freezing of birch pollen washing water, Atmos. Chem. Phys., 13, 10989–11003, doi:10.5194/acp-13-10989-2013, 2013.

Aylor, D. E.: Settling speed of corn (Zea mays) pollen, J. Aerosol Sci., 33, 1601–1607, 2002.

Cantrell, W. and Heymsfield, A.: Production of Ice in Tropospheric Clouds: A Review, B. Am. Meteorol. Soc., 86, 795–807, 2005.

Choi, M. Y. and Chan, C. K.: The Effects of Organic Species on the Hygroscopic Behaviors of Inorganic Aerosols, Environ. Sci. Technol., 36, 2422–2428, 2002.

Davis, E. J.: A history of single aerosol particle levitation, Aerosol Sci. Technol., 26, 212–254, 1997.

Davies, J. F., Haddrell, A. E., and Reid, J. P.: Time-Resolved Measurements of the Evaporation of Volatile Components from Single Aerosol Droplets, Aerosol Sci. Technol., 46, 666–677, 2012.

Davies, J. F., Miles, R. E. H., Haddrell, A. E., and Reid, J. P.: Influence of organic films on the evaporation and condensation of water in aerosol, P. Natl. Acad. Sci. USA, 110, 8807–8812, 2013.

Davies, J. F., Miles, R. E. H., Haddrell, A. E., and Reid, J. P.: Temperature dependence of the vapor pressure and evaporation coefficient of supercooled water, J. Geophys. Res.-Atmos., 119, 10931–10940, 2014.

Deguillaume, L., Leriche, M., Amato, P., Ariya, P. A., Delort, A.-M., Pöschl, U., Chaumerliac, N., Bauer, H., Flossmann, A. I., and Morris, C. E.: Microbiology and atmospheric processes: chemical interactions of primary biological aerosols, Biogeosciences, 5, 1073–1084, doi:10.5194/bg-5-1073-2008, 2008.

DeMott, P. J., Prenni, A. J., Liu, X., Kreidenweis, S. M., Petters, M. D., Twohy, C. H., Richardson, M. S., Eidhammer, T., and Rogers, D. C.: Predicting global atmospheric ice nuclei distributions and their impacts on climate, P. Natl. Acad. Sci. USA, 107, 11217–11222, 2010.

Després, V. R., Nowoisky, J. F., Klose, M., Conrad, R., Andreae, M. O., and Pöschl, U.: Characterization of primary biogenic aerosol particles in urban, rural, and high-alpine air by DNA sequence and restriction fragment analysis of ribosomal RNA genes, Biogeosciences, 4, 1127–1141, doi:10.5194/bg-4-1127-2007, 2007.

Diehl, K., Quick, C., Matthias-Maser, S., Mitra, S. K., and Jaenicke, R.: The ice nucleating ability of pollen. Part I: Laboratory studies in deposition and condensation freezing modes, Atmos. Res., 58, 75–87, 2001.

Diehl, K., Matthias-Maser, S., Jaenicke, R., and Mitra, S. K.: The ice nucleating ability of pollen: Part II. Laboratory studies in immersion and contact freezing modes, Atmos. Res., 61, 125–133, 2002.

Galanos, C., Lüderitz, O., and Westphal, O.: A new method for the extraction of R Lipopolysaccharides, Euro. J. Biochem., 9, 245–249, 1969.

Glantschnig, W. J. and Chen, S.-H.: Light scattering from water droplets in the geometrical optics approximation, Appl. Optics, 20, 2499–2509, 1981.

Griffiths, P. T., Borlace, J.-S., Gallimore, P. J., Kalberer, M., Herzog, M., and Pope, F. D.: Hygroscopic growth and cloud activation of pollen: a laboratory and modelling study, Atmos. Sci. Lett., 13, 289–295, 2012.

Haynes, W. M.: CRC Handbook of Chemistry and Physics, 94th Edition, CRC Press, Taylor & Francis Group, 6–164, 2013.

Heinisch, C., Bakić, C., Damaschke, N., Petter, J., Tschudi, T., and Tropea, C.: Neue Paulfallengeometrie Zur Fixierung Von Tropfen Und Partikeln In Gasströmungen Mit 360°-Zugang Für Laserdiagnostik. 14 Fachtagung Lasermethoden in der Strömungsmesstechnik, PTB, Braunschweig, 2.61–2.66, 2006.

Heinisch, C., Wills, J. B., Reid, J. P., Tschudi, T., and Tropea, C.: Temperature measurement of single evaporating water droplets in a nitrogen flow using spontaneous Raman scattering, Phys. Chem. Chem. Phys., 11, 9720–9728, 2009.

Heise, H. A. and Heise, E. R.: The distribution of ragweed pollen and alternaria spores in the upper atmosphere, J. Allergy, 19, 403–407, 1948.

Helbig, N., Vogel, B., Vogel, H., and Fiedler, F.: Numerical modelling of pollen dispersion on the regional scale, Aerobiologia, 3, 3–19, 2004.

Hirschfelder, J. O., Curtiss, C. F., and Bird, R. B.: Molecular theory of gases and liquids, John Wiley & Sons, Inc., New York, 1954.

Hoffmann, N., Duft, D., Kiseleva, A., and Leisner, T.: Contact freezing efficiency of mineral dust aerosols studied in an electrodynamic balance: quantitative size and temperature dependence for illite particles, Faraday Discuss., 165, 383–390, 2013a.

Hoffmann, N., Kiselev, A., Rzesanke, D., Duft, D., and Leisner, T.: Experimental quantification of contact freezing in an electrodynamic balance, Atmos. Meas. Tech., 6, 2373–2382, doi:10.5194/amt-6-2373-2013, 2013b.

Hogan, R. J., Behera, M. D., O'Connor, E. J., and Illingworth, A. J.: Estimate of the global distribution of stratiform supercooled liquid water clouds using the LITE lidar, Geophys. Res. Lett., 31, L05106, doi:10.1029/2003GL018977, 2004.

Holyst, R., Litniewski, M., Jakubczyk, D., Kolwas, K., Kolwas, M., Kowalski, K., Migacz, S., Palesa, S., and Zientara, M.: Evaporation of freely suspended single droplets: experimental, theoretical and computational simulations, Rep. Prog. Phys. 76, 034601, doi:10.1088/0034-4885/76/3/034601, 2013.

Hoose, C., Kristjánsson, J. E., and Burrows, S. M.: How important is biological ice nucleation in clouds on a global scale?, Environ. Res. Lett., 5, 024009, doi:10.1088/1748-9326/5/2/024009 2010.

Hoose, C. and Möhler, O.: Heterogeneous ice nucleation on atmospheric aerosols: a review of results from laboratory experiments, Atmos. Chem. Phys., 12, 9817–9854, doi:10.5194/acp-12-9817-2012, 2012.

Kanji, Z. A., Welti, A., Chou, C., Stetzer, O., and Lohmann, U.: Laboratory studies of immersion and deposition mode ice nucleation of ozone aged mineral dust particles, Atmos. Chem. Phys., 13, 9097–9118, doi:10.5194/acp-13-9097-2013, 2013.

Knopf, D. A., Alpert, P. A., Wang, B., and Aller, J. Y.: Stimulation of ice nucleation by marine diatoms, Nat. Geosci., 4, 88–90, 2011.

Koop, T., Luo, B., Tsias, A., and Peter, T.: Water activity as the determinant for homogeneous ice nucleation in aqueous solutions, Nature, 406, 611–614, 2000.

Krämer, B., Hübner, O., Vortisch, H., Wöste, L., and Leisner, T., Schwell, M., Rühl, E., and Baumgärtel, H.: Homogeneous nucleation rates of supercooled water measured in single levitated microdroplets, J. Chem. Phys., 111, 6521–6527, 1999.

Krieger, U. K., Colberg, C. A., Weers, U., Koop, T., and Peter, T.: Supercooling of single H_2SO_4/H_2O aerosols to 158 K: No evidence for the occurrence of the octahydrate, Geophys. Res. Lett., 27, 2097–2100, 2000.

Krieger, U. K., Marcolli, C., and Reid, J. P.: Exploring the complexity of aerosol particle properties and processes using single particle techniques, Chem. Soc. Rev., 41, 6631–6662, 2012.

Kulmala, M., Vesala, T., and Wagner, P. E.: An analytical expression for the rate of binary condensational particle growth, Proc. R. Soc. Lon. Ser. A, 441, 589–605, 1993.

Laaksonen, A., Talanquer, V., and Oxtoby, D. W.: NUCLEATION: Measurements, Theory, and Atmospheric Applications, Annu. Rev. Phys. Chem., 46, 489–524, 1995.

Ladino Moreno, L. A., Stetzer, O., and Lohmann, U.: Contact freezing: a review of experimental studies, Atmos. Chem. Phys., 13, 9745–9769, doi:10.5194/acp-13-9745-2013, 2013.

Lee, A. K. Y. and Chan, C. K.: Single particle Raman spectroscopy for investigating atmospheric heterogeneous reactions of organic aerosols, Atmos. Environ., 41, 4611–4621, 2007.

Lee, A. K. Y., Ling, T. Y., and Chan, C. K.: Understanding hygroscopic growth and phase transformation of aerosols using single particle Raman spectroscopy in an electrodynamic balance, Faraday Discuss., 137, 245–263, 2008.

Lee, J. W. L., Carrascón, V., Gallimore, P. J., Fuller, S. J., Björkegren, A., Spring, D. A., Pope, F. D., and Kalberer, K.: The effect of humidity on the ozonolysis of unsaturated compounds in aerosol particles, Phys. Chem. Chem. Phys., 14, 8023–8031, 2012.

Li, K.-Y., Tu, H., and Ray, A. K.: Charge Limits on Droplets during Evaporation, Langmuir, 21, 3786–3794, 2005.

Lohmann, U. and Feichter, J.: Global indirect aerosol effects: a review, Atmos. Chem. Phys., 5, 715–737, doi:10.5194/acp-5-715-2005, 2005.

Mason B. J.: Clouds and rainmaking, Cambridge University Press, Cambridge, UK, 1975.

Mie, G.: Beiträge zur Optik Trüber Medien, Speziell Kolloidaler Metallösungen, Ann. Phys., 25, 377–445, 1908.

Miles, R. E. H., Reid, J. P., and Riipinen, I.: Comparison of Approaches for Measuring the Mass Accommodation Coefficient for the Condensation of Water and Sensitivities to Uncertainties in Thermophysical Properties, J. Phys. Chem. A, 116, 10810–10825, 2012.

Möhler, O., DeMott, P. J., Vali, G., and Levin, Z.: Microbiology and atmospheric processes: the role of biological particles in cloud physics, Biogeosciences, 4, 1059–1071, doi:10.5194/bg-4-1059-2007, 2007.

Moller, B., Rarey, J., and Ramjugernath, D.: Estimation of the vapour pressure of non-electrolyte organic compounds via group contributions and group interactions, J. Mol. Liq., 143, 52–63, 2008.

Murphy, B. D. and Koop, T.: Review of the vapour pressures of ice and supercooled water for atmospheric applications, Q. J. Roy. Meteor. Soc., 131, 1539–1565, 2005.

Murray, B. J., Wilson, T. W., Dobbie, S., Cui, Z., Al-Jumur, S. M. R. K., Möhler, O., Schnaiter, M., Wagner, R., Benz, S., Niemand, M., Saathoff, H., Ebert, V., Wagner, S., and Kärcher.: Heterogeneous nucleation of ice particles on glassy aerosols under cirrus conditions, Nat. Geosci., 3, 233–237, 2010.

Murray, B. J., O'Sullivan, D., Atkinson, J. D., and Webb, M. E.: Ice nucleation by particles immersed in supercooled cloud droplets, Chem. Soc. Rev., 41, 6519–6554, 2012.

Parsons, M. T., Riffell, J. L., and Bertram, A. K.: Crystallization of aqueous inorganic-malonic acid particles: Nucleation rates, dependence on size, and dependence on the ammonium-to-sulfate, J. Phys. Chem. A, 110, 8108–8115, 2006.

Pope, F. D.: Pollen grains are efficient cloud condensation nuclei, Environ. Res. Lett., 5, 044015, doi:10.1088/1748-9326/5/4/044015, 2010.

Pope, F. D., Dennis-Smither, B. J., Griffiths, P. T., Clegg, S. L., and Cox, R. A.: Studies of Single Aerosol Particles Containing Malonic Acid, Glutaric Acid, and Their Mixtures with Sodium Chloride. I. Hygroscopic Growth, J. Phys. Chem. A, 114, 5335–5341, 2010a.

Pope, F. D., Tong H.-J., Dennis-Smither, B. J., Griffiths, P. T., Clegg, S. L., Reid, J. P., and Cox, R. A.: Studies of Single Aerosol Particles Containing Malonic Acid, Glutaric Acid, and Their Mixtures with Sodium Chloride. II. Liquid-State Vapor Pressures of the Acids, J. Phys. Chem. A, 114, 10156–10165, 2010b.

Pope, F. D., Gallimore, P. J., Fuller, S. J., Cox, R. A., and Kalberer, M.: Ozonolysis of maleic acid aerosols: Initial results on aerosol hygroscopicity and volatility, Environ. Sci. Technol., 44, 6656–6660, 2010c.

Pöschl, U.: Atmospheric Aerosol: Composition, Transformation, Climate and Health Effects, Angew. Chem. Int. Edit., 44, 7520–7540, 2005.

Pratt, K. A., DeMott, P. J., French, J. R., Wang, Z., Westphal, D. L., Heymsfield, A. J., Twohy, C. H., Prenni, A. J., and Prather, K. A.: In situ detection of biological particles in cloud ice-crystals, Nat. Geosci., 2, 398–401, 2009.

Pruppacher, H. R. and Klett, J. D.: Microphysics of Clouds and Precipitation, Atmospheric and Oceanographic Sciences Library, Kluwer Academic Press, Dordrecht, the Netherlands, 1997.

Pummer, B. G., Bauer, H., Bernardi, J., Bleicher, S., and Grothe, H.: Suspendable macromolecules are responsible for ice nucleation activity of birch and conifer pollen, Atmos. Chem. Phys., 12, 2541–2550, doi:10.5194/acp-12-2541-2012, 2012.

Pummer, B. G.: Ice nucleation activity of pollen and fungal spores, PhD Dissertation, Technische Universität Wien, 2013.

Pummer, B. G., Bauer, H., Bernardi, J., Chazallon, B., Facq, S., Lendl, B., Whitmore, K., and Grothe, H.: Chemistry and morphology of dried-up pollen suspension residues, J. Raman Spectrosc., 44, 1654–1658, 2013.

Rauber, R. M. and Tokay, A.: An Explanation for the Existence of Supercooled Water at the Top of Cold Clouds, J. Atmos. Sci., 48, 1005–1023, 1991.

Rosenfeld, D. and Woodley, W. L.: Deep convective clouds with sustained supercooled liquid water down to −37.5 °C, Nature, 405, 440–442, 2000.

Rousseau, D.-D., Duzer, D., Cambon, G, Jolly, D., Poulsen, U., Ferrier, J., Schevin, P., and Gros, R.: Long distance transport of pollen to Greenland, Geophys. Res. Lett., 30, 1765, doi:10.1029/2003GL017539, 2003.

Sassen, K.: Highly supercooled cirrus cloud water: confirmation and climatic implications, Science, 227, 411–413, 1985.

Schäppi, G. F., Taylor, P. E., Pain, M. C. F., Cameron, P. A., Dent, A. W., Staff, I. A., and Suphioglu, C.: Concentrations of major grass group 4 allergens in pollen grains and atmospheric particles: implications for hay fever and allergic asthma sufferers sensitized to grass pollen allergens, Clin. Exp. Allergy, 29, 633–641, 1999.

Seinfeld, J. H. and Pandis, S. N.: Atmospheric Chemistry and Physics: From Air Pollution to Climate Change, New York, Wiley, 1998.

Shaw, R. A., Lamb, D., and Moyle, A. M.: An Electrodynamic Levitation System for Studying Individual Cloud Particles under Upper-Tropospheric Conditions, J. Atmos. Ocean. Tech., 17, 940–948, 2000.

Sofiev, M., Siljamo, P., Ranta, H., and Rantio-Lehtimäki, A.: Towards numerical forecasting of long-range air transport of birch pollen: theoretical considerations and a feasibility study, Int. J. Biometeorol., 50 392–402, 2006.

Soonsin, V., Zardini, A. A., Marcolli, C., Zuend, A., and Krieger, U. K.: The vapor pressures and activities of dicarboxylic acids reconsidered: the impact of the physical state of the aerosol, Atmos. Chem. Phys., 10, 11753–11767, doi:10.5194/acp-10-11753-2010, 2010.

Stöckel, P., Weidinger, I. M., Baumgärtel, H., and Leisner, T.: Rates of Homogeneous Ice Nucleation in Levitated H_2O and D_2O Droplets, J. Phys. Chem. A, 109, 2540–2546, 2005.

Stratmann, F., Kiselev, A., Wurzler, S., Wendisch, M., Heintzenberg, J., Charlson, R. J., Diehl, K., Wex, H., and Schmidt, S.: Laboratory studies and numerical simulations of cloud droplet formation under realistic supersaturation conditions, J. Atmos. Ocean. Tech., 21, 876–887, 2004.

Svensson, E. A., Delval, C., von Hessberg, P., Johnson, M. S., and Pettersson, J. B. C.: Freezing of water droplets colliding with kaolinite particles, Atmos. Chem. Phys., 9, 4295–4300, doi:10.5194/acp-9-4295-2009, 2009.

Swanson, B. D., Bacon, N. J., Davis, E. J., and Baker, M. B.: Electrodynamic trapping and manipulation of ice crystals, Q. J. Roy. Meteor. Soc., 125, 1039–1058, 1999.

Tang, I. N. and Munkelwitz, H. R.: Water activities, densities, and refractive indices of aqueous sulfates and sodium nitrate droplets of atmospheric importance, J. Geophys. Res., 99, 18801–18808, 1994.

Tong, H.-J., Reid, J. P., Bones, D. L., Luo, B. P., and Krieger, U. K.: Measurements of the timescales for the mass transfer of water in glassy aerosol at low relative humidity and ambient temperature, Atmos. Chem. Phys., 11, 4739–4754, doi:10.5194/acp-11-4739-2011, 2011.

Vortisch, H. Krämer, B., Weidinger, I., Wöste, L., Leisner, T., Schwell, M. Baumgärtel, H., and Rühl, E.: Homogeneous freezing nucleation rates and crystallization dynamics of single levitated sulfuric acid solution droplets, Phys. Chem. Chem. Phys., 2, 1407–1413, 2000.

Yttri, K. E., Dye, C., and Kiss, G.: Ambient aerosol concentrations of sugars and sugar-alcohols at four different sites in Norway, Atmos. Chem. Phys., 7, 4267–4279, doi:10.5194/acp-7-4267-2007, 2007.

Zhang, Y. H. and Chan, C. K.: Study of Contact Ion Pairs of Supersaturated Magnesium Sulfate Solutions using Raman Scattering of Levitated Single Droplets, J. Phys. Chem. A., 104, 9191–9196, 2000.

Zobrist, B., Soonsin, V., Luo, B. P., Krieger, U. K., Marcolli, C., Peter, T., and Koop, T.: Ultra-slow water diffusion in aqueous sucrose glasses, Phys. Chem. Chem. Phys., 13, 3514–3526, 2011.